Volume 53
Number 4
28 January 2024
Pages 1357-1880

Dalton Transactions

An international journal of inorganic chemistry

rsc.li/dalton

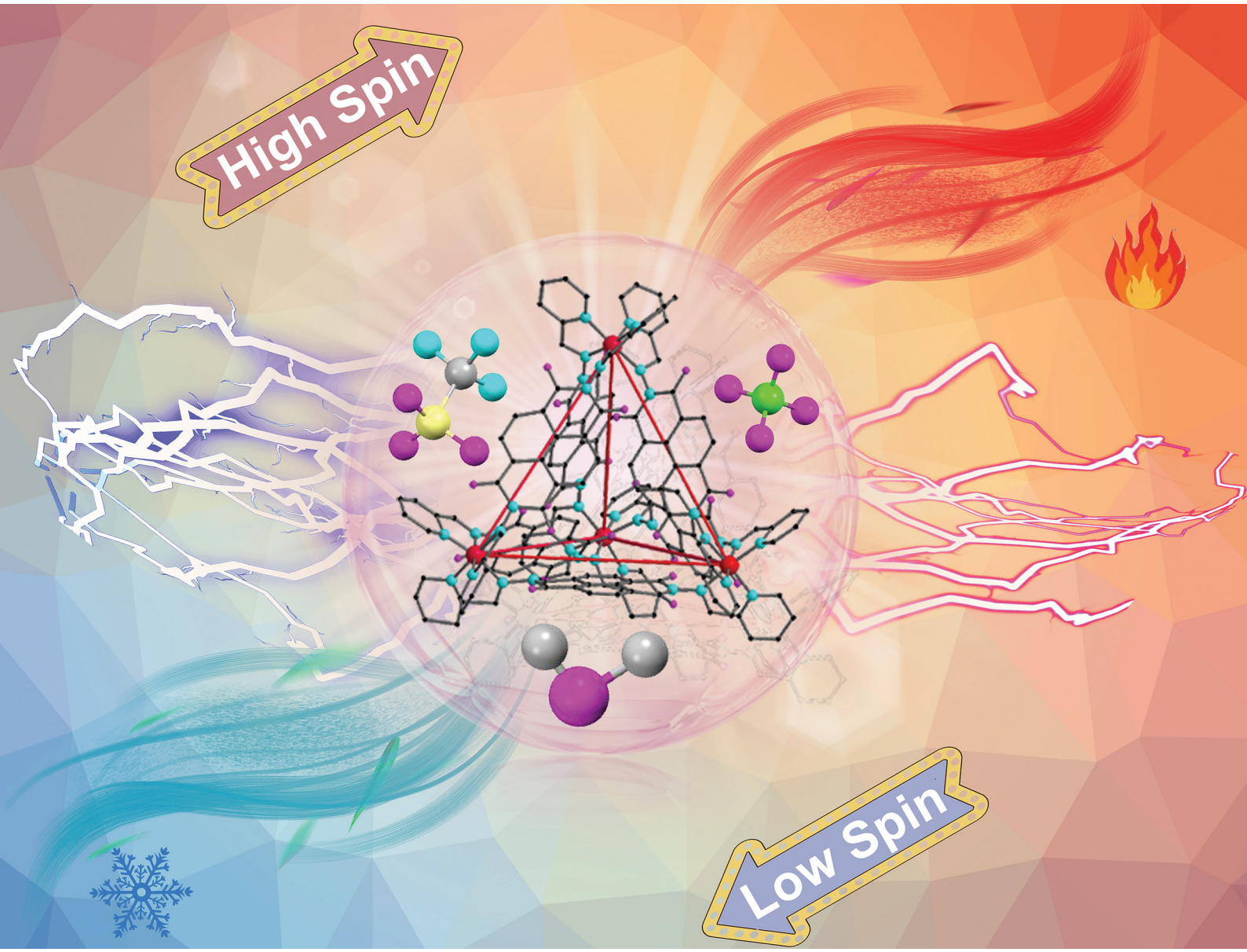

ISSN 1477-9226

ROYAL SOCIETY OF CHEMISTRY

PAPER

Yann Garcia *et al.*

Spin-state versatility in $Fe^{II}_4L_6$ supramolecular cages with a pyridyl-hydrazone ligand scaffold modulated by solvents and counter anions

Dalton Transactions

ROYAL SOCIETY OF CHEMISTRY

PAPER

View Article Online
View Journal | View Issue

Cite this: *Dalton Trans.*, 2024, **53**, 1449

Spin-state versatility in $Fe^{II}_4L_6$ supramolecular cages with a pyridyl-hydrazone ligand scaffold modulated by solvents and counter anions†

Weiyang Li,[a] Xiaochun Li,[a] Koen Robeyns,[a] Mariusz Wolff,[b] Joseph Kfoury,[c] Julianna Oláh,[c] Radovan Herchel,[d] Serhiy Demeshko,[e] Franc Meyer[e] and Yann Garcia *[a]

Discrete spin crossover (SCO) tetranuclear cages are a unique class of materials that have potential use in next-generation molecular recognition and sensing. In this work, two new edge-bridged SCO $Fe^{II}_4L_6$ (L = 2,7-bis(((*E*)-pyridin-2-ylmethylene)amino)benzo[*lmn*] [3,8]phenanthroline-1,3,6,8(2*H*,7*H*)-tetraone) supramolecular cages with different counter anions: ClO_4^- (**2**) and $CF_3SO_3^-$ (**3**) were constructed *via* subcomponent self-assembly to investigate both solvent and anion influences on their magnetic properties and compare them to cage **1** with a BF_4^- anion. Pyridyl-hydrazone bidentate ligand scaffolds were employed to replace the 'classical' imidazole/thiazolyl-imine coordination units to induce SCO behaviour in these cages. **2** and **3** were structurally characterized by single-crystal X-ray diffraction analysis and electrospray ionization time-of-flight mass spectrometry. Magnetic susceptibilities of **1–3** and **1–3**·desolvated indicate that the solvents' presence is in favor of the low-spin (LS) state. While different counter anions in **1–3**·desolvated affect the spin-state configurations of the four Fe^{II} metal centers. According to the ^{57}Fe Mössbauer spectral analysis, the spin-state distributions in **1–3** at 80 K are [2 high-spin (HS)–2LS], [1HS–3LS] and [2HS–2LS], respectively and density functional theory calculations were employed to investigate the reasons. These findings provide insights to regulate the spin-state versatility of SCO Fe^{II} cage systems in the solid state.

Received 1st August 2023,
Accepted 18th October 2023

DOI: 10.1039/d3dt02474a

rsc.li/dalton

Introduction

Fe^{II} spin crossover (SCO) complexes have attracted enormous attention due to their potential applications in information memories, nano-electronics/spintronics and sensors.[1,2] The reversible spin transition between paramagnetic high-spin (HS) and diamagnetic low-spin (LS) states can be achieved by exposure to external physico-chemical stimuli such as variations in temperature, pressure, light irradiation and guest chemical modification.[3,4] So far, the design and synthesis methods of mononuclear Fe^{II} SCO complexes with FeN_6 pseudo-octahedral coordination geometry have been systematically studied because of their somewhat simplified ligand conformations as well as structures.[5,6] However, research on polynuclear (from binuclear to octanuclear) Fe^{II} SCO compounds is still in the exploratory phase.[7] In particular, the tetranuclear tetrahedral molecular cages have attracted a great deal of interest because of the presence of well-defined central cavities, which offer the possibility of altering the SCO behavior *via* host–guest interaction.[8,9] Meanwhile, the specific recognition of guest molecules due to size effects or steric hindrance in the cavity could induce variations in spin states[10] and optical properties, which may turn the SCO cages into colorimetric sensors.[11] In addition, the usual requirements for molecular storage devices involve the need for two stable spin states, while Fe^{II} SCO cage compounds theoretically have accessibility up to five spin states, *i.e.*, $(Fe^{II}LS)_n(Fe^{II}HS)_{4-n}$ (n = 0–4).[12]

In 2013, Kruger *et al.* presented the first face-capped $Fe^{II}_4L_4$ SCO cage, replacing the 2,2-bipyridine and pyridine-imine coordination sites normally employed in the construction of LS tetrahedral cages with imidazole-imine sites, as imidazole N atoms typically possess weaker ligand field strengths than

[a]*Institute of Condensed Matter and Nanosciences, Molecular Chemistry, Materials and Catalysis (IMCN/MOST), Université catholique de Louvain, Place Louis Pasteur 1, 1348 Louvain-la-Neuve, Belgium. E-mail: yann.garcia@uclouvain.be*
[b]*Institut für Chemische Katalyse, Fakultät für Chemie, Universität Wien, Währinger Strasse 38, 1090 Wien, Austria*
[c]*Department of Inorganic and Analytical Chemistry, Budapest University of Technology and Economics, H-1111 Szent Gellért tér 4, Budapest, Hungary*
[d]*Department of Inorganic Chemistry, Faculty of Science, Palacký University, 17. listopadu 12, 77146 Olomouc, Czech Republic*
[e]*Institut für Anorganische Chemie, Universität Göttingen, Tammannstrasse 4, D-37077 Göttingen, Germany*

†Electronic supplementary information (ESI) available. CCDC 2270896 and 2270897. For ESI and crystallographic data in CIF or other electronic format see DOI: https://doi.org/10.1039/d3dt02474a

pyridine N atoms.[13,14] After that, the 'classical' imidazole-imine ligand scaffolds have been widely used for inducing SCO behavior in Fe^{II} tetrahedral cages by Nitschke,[15] Gu,[10,16–18] Li[19] and Suzuki.[20] In 2019, Li and coworkers developed an edge-bridged $Fe^{II}_4L_6$ SCO cage with thiazolyl–imine coordination sites exhibiting hysteresis phenomenon up to 29 K.[21] Clearly, the ligand scaffold is a critical factor in the realization or modification SCO behaviors in Fe^{II} cage systems, but proposing a new coordination motif remains challenging due to the difficulty in matching the appropriate ligand field and coordination geometry to achieve desired SCO properties. Also, the acquisition of single crystals for the cages and the determination of the crystal structure (often containing large amounts of disordered solvents or anions within the cavity) are additional challenges.[12] For these reasons, the Fe^{II} SCO cages development is still in its relative infancy.[7] To date, only nine papers (excluding our recent communication[22]) have reported SCO cages in the solid state, resulting in 15 crystal structures, 14 of which used the imidazole–imine coordination sites and one cage used the thiazolyl–imine coordination sites.[10,13,15–21] All ligands reported in literature for the construction of SCO tetrahedral cages are summarized in Scheme 1. The average Fe–Fe lengths, cavity volumes, CCDC numbers and counter anions position (inside or outside cavities) of all reported SCO cages are summarized in Table S1.†

Recently, we developed the first $Fe^{II}_4L_6$ SCO cage (**1**, Scheme 2) constructed with a pyridyl-hydrazone coordination core, which is usually used for constructing SCO $Fe^{II}_4L_4$ grids and $Fe^{II}L_2$ mononuclear complexes.[22] However, the SCO profile is gradual, incomplete and without hysteresis loop, which limits any potential applicability in data storage devices.[22] It is known from literature that two factors, namely solvents and counter anions, are crucial in determining the magnetic behavior of SCO materials.[23,24] For instance, Kruger *et al.* reported an interesting mononuclear Fe^{II} complex that exhibits a broad two-step full SCO behaviour in the presence of solvents, while its corresponding desolvated phase converts to a sharp one-step SCO accompanied by a thermal hysteresis

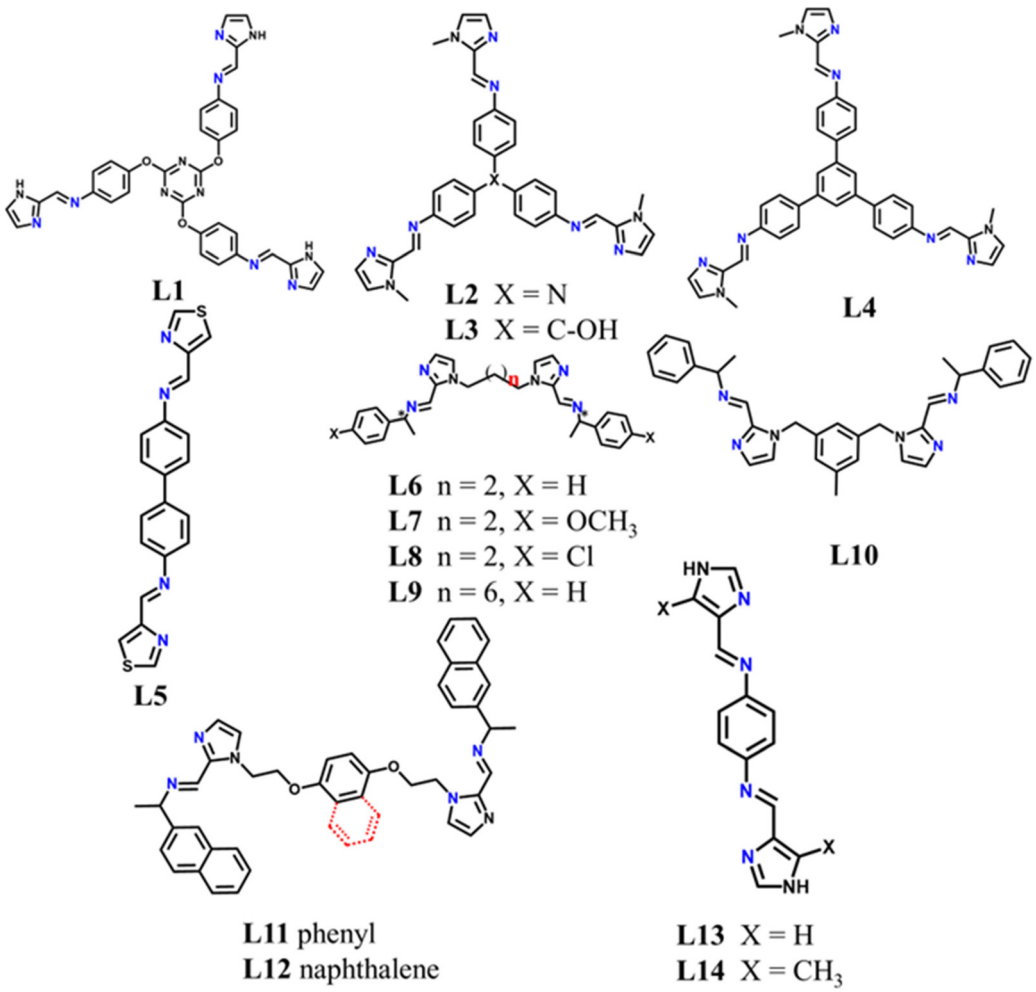

Scheme 1 Reported ligands used to construct SCO tetrahedral cages. For **L6–L8**, both the (*R*,*R*) and (*S*,*S*) configurations at the chiral (*) center were used to form cages. $[Fe_4(L2)_4](CF_3SO_3)_8$ and $[Fe_4(L8)_6](ClO_4)_8$ (*R*) were not structurally determined, while the cages formed by the other ligands all have crystal structures (15 in total).

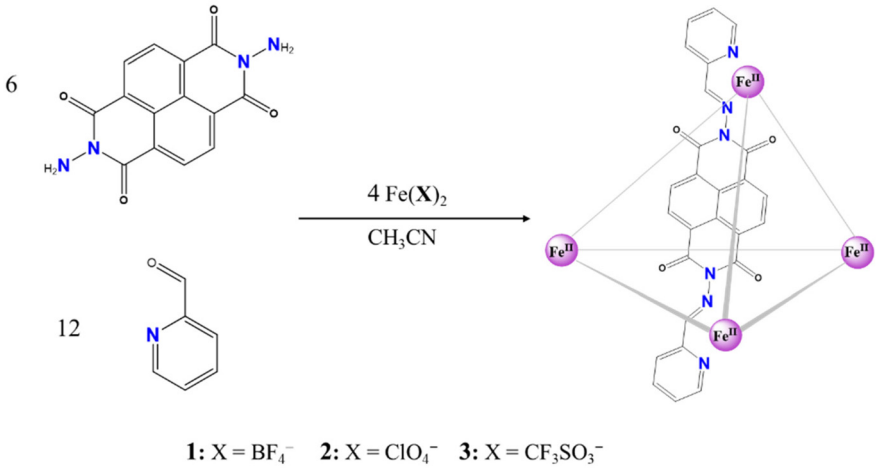

1: X = BF_4^- **2:** X = ClO_4^- **3:** X = $CF_3SO_3^-$

Scheme 2 Synthetic strategy for the preparation of **1–3**.

(10 K).[25] Garcia *et al.* demonstrated two linear regimes between the volume of the inserted counterions and the transition temperature ($T_{1/2}$) of the $[Fe(Rtrz)_3]^{2+}$ (R = 4-amino-1,2,4-triazole) one-dimensional polymer chains, *i.e.*, when the volume is between 0.04 nm^3 and 0.09 nm^3, $T_{1/2}$ decreases as the volume increases; when the volume exceeds 0.11 nm^3, $T_{1/2}$ tends to saturate (~200 K).[26] However, the influence of these two factors on SCO profiles in Fe^{II} discrete polynuclear systems has been relatively little investigated compared to mononuclear and polymeric complexes.[27] Among them, binuclear $Fe^{II}_2L_3$ helicates[28–31] and tetranuclear $Fe^{II}_4L_4$ grid complexes[23,32,33] are comparatively well established, but tetranuclear cage systems have not been investigated up to now.

In this study, we attempted to investigate the solvent and counter anion effects on SCO behaviour compared to cage **1**. Two new Fe^{II} tetrahedral cages were synthesized through subcomponent self-assembly using the same pyridine–hydrazone ligand scaffold but with different counter anions ClO_4^- (**2**) and $CF_3SO_3^-$ (**3**) (Scheme 2). The structures of **2** and **3** have been confirmed by single-crystal X-ray diffraction and electrospray ionization time-of-flight mass spectrometry (ESI-TOF-MS), and their magnetic properties were carefully investigated by SQUID magnetometry and ^{57}Fe Mössbauer spectroscopy. Magnetic data indicate that the solvents presence in **1–3** stabilize the LS state, while different counter anions in **1–3** affect the spin-state configuration of the four Fe^{II} metal centers. This work provides insights into the design of a new type of Fe^{II} SCO cages and may also serve as a reference for chemists aiming to tune the multiple spin-state distribution in tetranuclear Fe^{II} cage systems.

Results and discussion

Synthesis

The subcomponent ligand *N*,*N*-diaminonaphthalene-1,4,5,8-tetracarboxydi-imide was synthesized through a condensation reaction in acetone.[34] Cage **2** and **3** were prepared by subcomponent self-assembly, which is a well implemented tool to simplify ligand and complex supramolecular cage structures synthesis through forming dynamic covalent (C═N) and coordinative (N → M) bonds.[35] Six equivalents of *N*,*N*-diaminonaphthalene-1,4,5,8-tetracarboxydi-imide were mixed with 12 equivalents of 2-formylpyridine and 4 equivalents of Fe $(ClO_4)_2{\cdot}6H_2O$ or $Fe(CF_3SO_3)_2$ in acetonitrile and heated at 65 °C under $Ar_{(g)}$ both giving purple solutions, corresponding to **2** and **3**, respectively (Scheme 2, see ESI†). After filtration, diethyl ether was slowly diffused into the filtrate over a period of time at room temperature, producing single crystals suitable for X-ray crystallographic analysis. Notably, the crystals of **2** and **3** are quite small and unstable, *i.e.*, they readily redissolved into acetonitrile as the ether evaporated during harvesting of the crystals. To be able to manipulate the crystals prior to data collection, transferring the crystals to a high boiling point solvent, such as tetrahydrofuran or isopropyl ether, could effectively alleviate this issue.[22] We also tried some Fe^{II} salts with other counter anions, such as $FeCl_2{\cdot}4H_2O$, $FeBr_2$, $FeSO_4{\cdot}7H_2O$, and $[Fe(H_2O)_6](psca)_2{\cdot}2H_2O$ (psca = *para*-sulfocinnamic acid) but found that the reactants did not form a clear solution in acetonitrile. Furthermore, based on literature research, only these three anions (BF_4^-, ClO_4^- and $CF_3SO_3^-$) were utilized in the majority of Fe^{II}-based supramolecular cages characterized by single crystal X-ray diffraction.[7,9]

Crystal structure of 2

Single-crystal X-ray diffraction (SXRD) analysis performed upon red-block crystals of **2** at 120 K revealed the complex crystallized in the triclinic $P\bar{1}$ space group with a unit cell volume of 8837.4(13) $Å^3$ (Z = 2). The detailed crystallographic and refinement data are summarized in Table 1. As shown in Fig. 1a, the Fe^{II} cage is constructed of four metal centers occupying the apex of the tetrahedron and six ligands located at the edges of the tetrahedron, forming an edge-bridged configuration. Each Fe^{II} ion is found to be coordinated with six

Table 1 Crystal data and structure refinement details for **2** and **3**

Sample	**2**	**3**
T (K)	120	100
Formula	$C_{156}H_{84}Fe_4N_{36}O_{24}\cdot 8(ClO_4)\cdot 3(C_2H_3N)$ [+solvent]	$[C_{156}H_{84}Fe_4N_{36}O_{24}]_2\cdot 13(CF_3SO_3)\cdot 11(C_2H_3N)$ [+solvent]
Formula weight	3988.75	8529.48
Radiation (Å)	MoK_α (0.71073)	MoK_α (0.71073)
Crystal system	Triclinic	Monoclinic
Space group	$P\bar{1}$	Ia
a (Å)	16.7950(17)	28.3061(4)
b (Å)	16.8250(12)	22.1383(2)
c (Å)	33.0377(19)	70.1304(9)
α (°)	75.558(6)	90
β (°)	78.046(7)	98.3311(13)
γ (°)	89.230(7)	90
V (Å^3)	8837.4(13)	43 483.4(10)
Z	2	4
ρ_{calc} (g cm^{-3})	1.499	1.303
Absorption coefficient (mm^{-1})	0.541	0.418
θ range (°)	2.513 to 20.815	2.854 to 25.697
F(000)	4054	17 308
Crystal size (mm)	0.1 × 0.08 × 0.01	0.12 × 0.1 × 0.02
Reflections collected	34 789	239 369
Independent reflections	17 635 [$R_{(int)}$ = 0.0809]	78 695 [$R_{(int)}$ = 0.0601]
Data/restraints/parameters	17 635/673/2514	78 695/1859/5206
Goodness of fit on F^2	1.282	1.141
R_1, wR_2 ($I > 2\sigma(I)$)	0.0951, 0.2111	0.0748, 0.1880
R_1, wR_2 (all data)	0.1684, 0.2373	0.0883, 0.1987

nitrogen atoms (FeN_6 geometry) from three bidentate pyridine–hydrazone binding pockets. The Fe–N coordination bond lengths vary from 1.96 Å to 1.99 Å, suggesting that the Fe^{II} centers are in the LS state at 120 K (Table S2†).[36] The average octahedral distortion parameter (Σ) for Fe^{II} centers is equal to 62.82° (defined as the sum of deviations from 90° of the 12 Fe–N *cis* angles; Σ = 0° is the ideal octahedron and increases with the degree of deformation[28]). Similar Σ value can be observed in reported Fe^{II} SCO tetranuclear cages with N_6 coordination cores in LS state.[7] The average Fe–Fe distance within tetrahedron is 12.63 Å (Fig. S1†). Eight ClO_4^- anions were present in the asymmetric unit, two of which were disordered and all located around the cage, with no anions found inside the cavity. The pyridine C–H in the ligand systems interact with the terminal O atoms in ClO_4^- anions or the O atoms in ketone group to form C–H···O interactions that link the neighboring cages (Fig. 1b). In the crystal packing viewed along the *a*-axis, the tetranuclear units are arranged in parallel sheets, forming a clear porous structure (Fig. 1c).

Crystal structure of 3

SXRD analysis at 100 K revealed that **3** crystallized in the monoclinic *Ia* space group and the unit cell volume is 43 483.4 (10) Å^3 with Z = 4. Two Fe^{II} cages were observed in the asymmetric unit, yet only thirteen $CF_3SO_3^-$ anions could be located in the electron density out of 16 excepted anions for the eight Fe^{II} ions. The remaining 3 anions reside in the large solvent cavity (>25% of the unit cell volume) and are most likely disordered. The tetranuclear complex **3** has a similar tetrahedral $Fe^{II}_4L_6$ configuration as in **2**, with a RMS deviation of about 0.28 Å^2 between them (Fig. 2a). The Fe–N bond distances at 100 K range from 1.97 Å to 2.00 Å, in agreement with a LS Fe^{II} electronic configuration (Table S3†).[36] **3** yielded a Σ value of 62.76°, indicating a similar irregularity degree of the octahedron geometry to that of **2**. The average intra-tetrahedral Fe–Fe distance in **3** is 12.29 Å (Fig. S2†), slightly shorter than that found in **2**. OTf^- anions bridging two adjacent cages by C–H···O interactions can also be observed in **3** (Fig. 2b). The crystal lattice creates interplanar spaces in the form of zigzag channels (Fig. 2c).

Characterization of 2 and 3

The tetranuclear nature of **2** and **3** was further demonstrated from ESI-TOF-MS measurements, which revealed a series of species with charge states varying from 3+ to 8+ owing to the successive loss of counterions and the experimental isotopic patterns matched well with simulated results (Fig. S3 and S4†). For example, in cage **2**, ion peaks at m/z 1189.0433, 866.7963, 673.6477, 452.7633 and 383.6741 are assigned to $[Fe_4L_6(ClO_4)_5]^{3+}$ $[Fe_4L_6(ClO_4)_4]^{4+}$, $[Fe_4L_6(ClO_4)_3]^{5+}$, $[Fe_4L_6(ClO_4)]^{7+}$, and $[Fe_4L_6]^{8+}$ species, respectively (Fig. S3b–S3f†). As shown in Fig. 3a, the Fourier-transform infrared (FT-IR) spectra of **2** and **3** show typical stretching of the C=N functional groups at 1584 cm^{-1} from pyridyl-imine.[22] The absorption bands centred at 1054 cm^{-1} in **2** reveals the existence of ClO_4^- anions, while the peaks at 1028 and 637 cm^{-1} in **3** are ascribed to the vibration of $CF_3SO_3^-$ anions.[17,37] Scanning electron microscopy equipped with energy dispersive spectroscopy (SEM-EDS) was employed to study micro morphologies and elemental distributions. **2** showed a regular rhombic block morphology (Fig. 3b), while **3** exhibited an irregular rectangular shape (Fig. 3c). C, O, N, Cl, Fe elements in **2** (Fig. S5†) and C, O, N, F, S, Fe elements in **3** (Fig. S6†) were detected in the EDS, and no impurity signals were observed. The UV diffuse reflectance spectra (DRS) of **2** and **3** in the

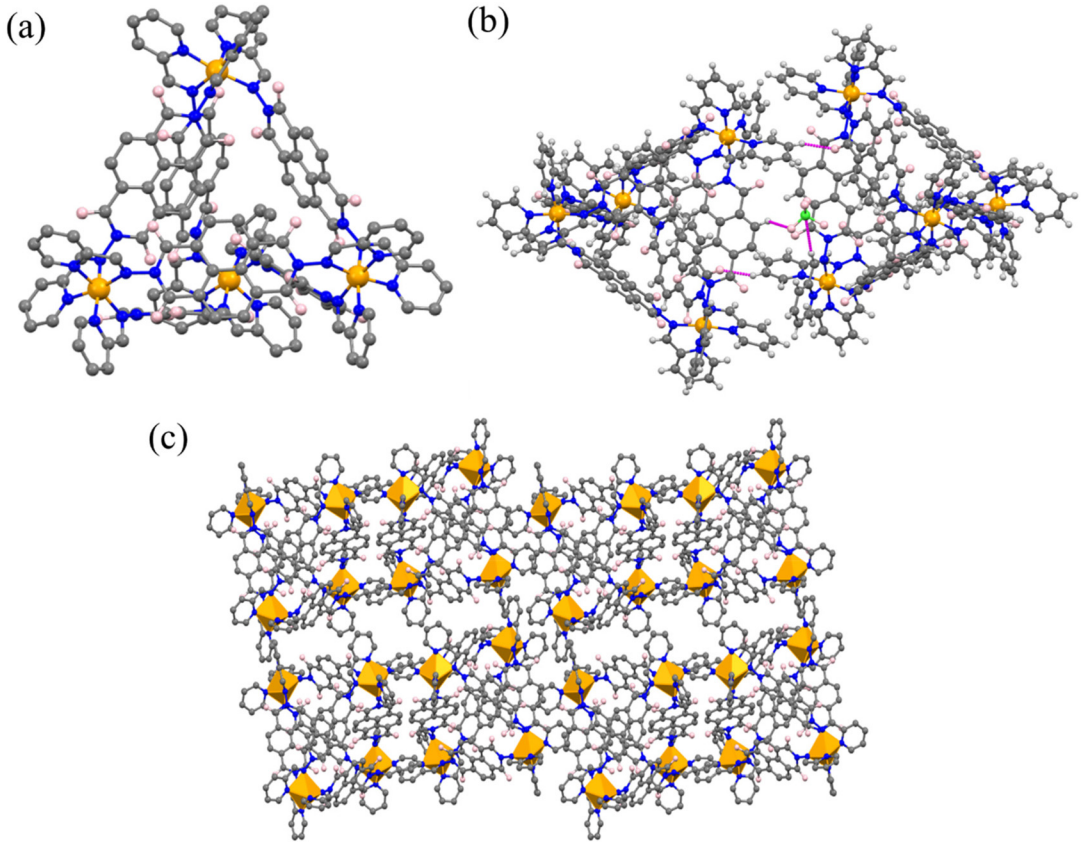

Fig. 1 (a) Molecular structure of **2** in solid state at 120 K, all hydrogen atoms, solvents molecules and counter anions have been omitted for clarity; (b) schematic representation of C–H···O interactions in **2** linking neighboring cages; (c) crystal packing based on polyhedral-model viewed along the *a*-axis. Color code: C-dark grey; N-blue; H-light grey; Fe-orange; O-pink; Cl-green.

solid-state exhibit similar absorption bands, *i.e.* intense bands at λ = 385 nm as well as relative weak broad bands centered at around λ = 540 nm (Fig. S7†). The former is likely arising from the ligand-centered π–π^* transitions, while the latter is assigned to the metal-to-ligand charge transfer (MLCT) transition, which features the coordination of Fe^{II} centers to imidazole–imine or pyridyl-hydrazone-based large aromatic ligands.[17,22] The thermogravimetric analysis (TGA) indicated that the thermal stability of **3** exceeds 250 °C, which is similar to **1**, while for cage **2** no high temperature analysis was performed due to the potential explosion risk of perchlorate[38] (Fig. S8 and S9†).

Solvent effects on the SCO properties

To investigate solvent effects on the SCO properties, DC magnetic susceptibility experiments were performed on **1–3** and *in situ* obtained **1–3**·desolvated at different temperature ranges. Since solvent effects on the SCO properties of these cages are similar (Fig. 4 and Fig. S10†), we shall only detail the ones of **2**. Given the high solubility of fresh crystals of **2** in acetonitrile, these were rinsed several times with an antisolvent (diethyl ether) and dried in the air, prior to SQUID measurements. The molecular formula of **2** was confirmed by elemental analysis and TGA (Fig. S8†) as $Fe^{II}_4L_6(ClO_4)_8{\cdot}10H_2O$. The presence of water molecules is presumably due to the fact that the cage adsorbs water molecules from air through hydrogen bonding during the drying process, *i.e.*, OH···O and OH···N, given that the ligand structures of these cages are rich in both oxygen and nitrogen atoms. As shown in the black curve of Fig. 4, the χ_mT value of **2** gradually decreases from 5.24 $cm^3\ mol^{-1}$ K at 300 K to 2.27 $cm^3\ mol^{-1}$ K at 50 K, indicating that approximately one Fe^{II} center has undergone a spin state transition from HS to LS, as the expected spin-only χ_mT value of one HS Fe^{II} ion is 3 $cm^3\ mol^{-1}$ K.[39] The subsequent heating curve from 2 to 300 K overlaps well with the cooling curve, demonstrating that the SCO behavior is reversible and without hysteresis for **2**. After annealing at 400 K, the non-solvated compound $Fe^{II}_4L_6(ClO_4)_8$ (**2**·desolvated) was obtained. The χ_mT value at 400 K is 11.05 $cm^3\ mol^{-1}$ K, however the shape of the curve (no plateau detected) shows that the cage is not in the full HS state. As the temperature is lowered, the χ_mT product again gradually decreases, with a trend similar to that of **2**. At 50 K, the χ_mT product is 3.42 $cm^3\ mol^{-1}$ K, suggesting that one Fe^{II} center remained in the HS state, *i.e.* [1HS–3LS], while about two Fe^{II} centers experienced SCO during the cooling process. The slight decrease in χ_mT below 20 K for both samples is likely attributed to zero-field splitting of HS

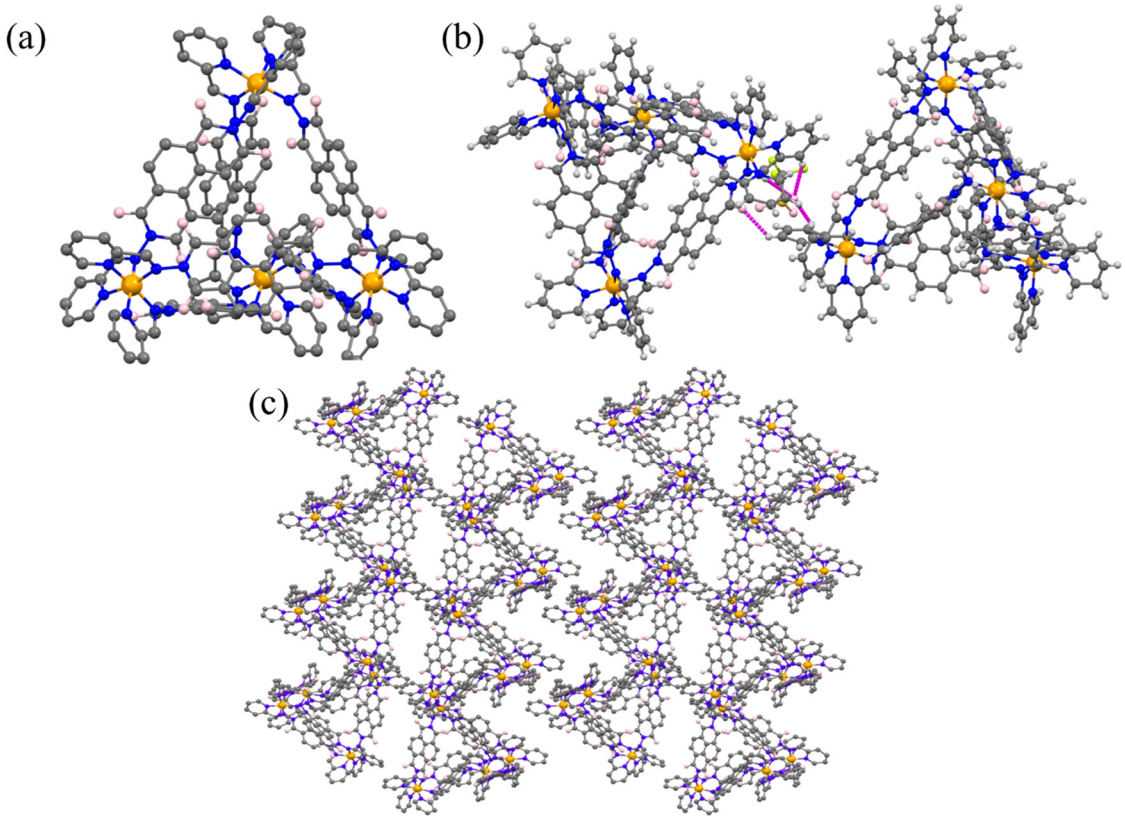

Fig. 2 (a) Molecular structure of **3** in solid state at 100 K, all hydrogen atoms, solvents molecules and counter anions have been omitted for clarity; (b) schematic representation of C–H···O interactions in **3** linking neighboring cages; (c) crystal packing based on ball and stick style viewed along the *b*-axis. Color code: C-dark grey; N-blue; H-light grey; Fe-orange; O-pink; F-yellow.

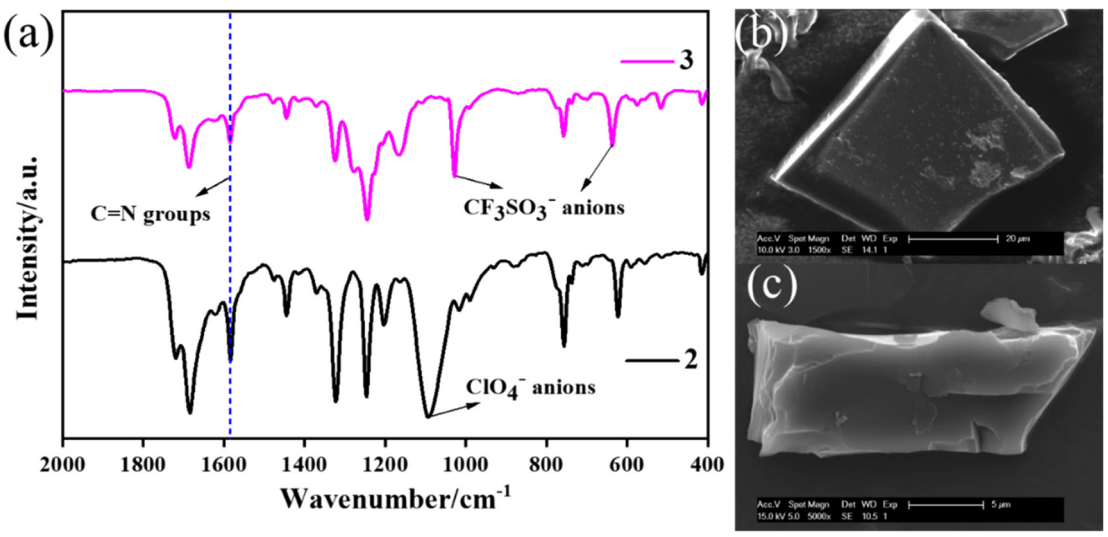

Fig. 3 (a) FT-IR spectra for **2** and **3**; SEM images of **2** (b) and **3** (c).

Fe^{II} ions.[39] Similarly, no hysteresis effect was observed in the magnetic profile. Thus, the presence of solvent molecules stabilizes the LS state, as indicated by the lower $\chi_m T$ values at the same temperature compared to **2**·desolvated, but overall without a significant effect on the SCO profile. Magnetic data for **1** and **3** exhibited similar results (Fig. S10†). This phenomenon is presumably attributed to the guest effect in SCO supramolecular cage compounds, in which water molecules form

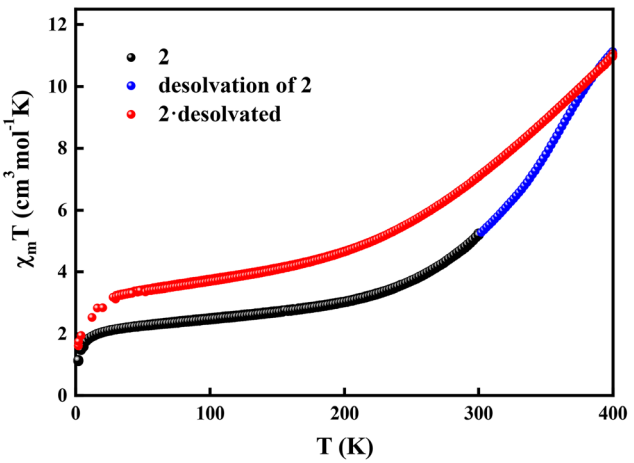

Fig. 4 Temperature dependence of the $\chi_m T$ product for **2** (black circles; 300–2–300 K), desolvation of **2** in the SQUID chamber (blue circles; 302–400 K) and **2**·desolvated (red circles; two cooling and heating cycles in the range of 400–2 K).

weak interactions such as hydrogen bonds with N (pyridyl-hydrazone groups) or O (ketone groups) atoms in the ligand system near the Fe^{II} centers, thus changing the electronic environment around the Fe^{II} nucleus and affecting its spin state.[16,24] Previous studies performed on analogous SCO Fe^{II} cage compounds demonstrated a similar trend.[13,16]

Anion effects on the SCO properties

To investigate the counter anion effects on the magnetic properties of the new tetranuclear cage family, complexes **1–3** with different anions (BF_4^-, ClO_4^- and $CF_3SO_3^-$ respectively) were prepared. All samples were annealed at 400 K within the SQUID cavity to rule out any solvent effect on the SCO properties.

As shown by the green plot of Fig. 5, the $\chi_m T$ value for **3** is 12.40 $cm^3\ mol^{-1}\ K$ at 400 K, decreasing to 6.03 $cm^3\ mol^{-1}\ K$ at 50 K as the temperature decreases, presumably due to a SCO from HS to LS states of Fe^{II} ions. The decrease in $\chi_m T$ below 20 K is ascribed to zero-field splitting of the HS Fe^{II} ions.[39] Hysteresis phenomenon was also not observed during the two rounds of heating and cooling processes in **3**. In addition, the $\chi_m T$ product at 50 K indicates approximately two Fe^{II} centers are present in the LS state, *i.e.* [2HS–2LS], similar to **1** but with one more HS center compared to **2**. Thus, from the magnetic data is evident that the counter anions influence the spin-state distribution of the four Fe^{II} ions, *e.g.* at 80 K the spin states of the desolvated form of **1**, **2** and **3** are [2HS–2LS], [1HS–3LS] and [2HS–2LS], respectively. Density functional theory calculations were used to investigate the causes of this phenomenon (*vide infra*). Furthermore, we noticed that the anion change did not effectively enhance the cooperativity in the system leading to no significant modification in the SCO profiles. This may be due to the fact that the anions are not located in the internal cavities of **1–3** and therefore the host–guest interaction is weak, not sufficient to cause any structural changes (Fe–N bond length) or alter the geometry of the metal ion in the cages during the spin transition.[8,40] Also, the volume of the counter anions is not directly related to the distribution of the spin states, as the volumes of BF_4^- (53 $Å^3$) and $CF_3SO_3^-$ (85 $Å^3$) differ significantly, but the spin states of the Fe^{II} ions are analogous, unlike the pattern observed in the $[Fe(4\text{-amino-}1,2,4\text{-triazole})_3]^{2+}$ 1D polymer chain[26] and tetranuclear grid systems.[33]

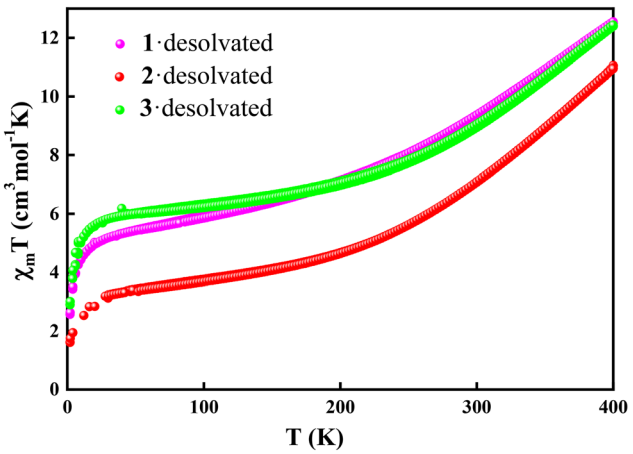

Fig. 5 Temperature dependence of the $\chi_m T$ product for desolvated **1–3** in the range 400–2 K (two cycles of cooling and warming).

To further investigate the spin state distribution, ^{57}Fe Mössbauer spectroscopy was conducted at 80 K on desolvated **1–3** samples. The spectrum of **2**·desolvated shows two quadrupole doublets (Fig. 6b). The first doublet with blue color exhibits an isomer shift of δ = 0.45 mm s^{-1} and a quadrupole splitting ΔE_Q = 0.36 mm s^{-1}, which is characteristic of LS Fe^{II} ions with an area fraction (A) of 80%.[4] The second doublet with red color [δ = 1.19 mm s^{-1}; ΔE_Q = 3.09 mm s^{-1}; A = 20%] is assigned to HS Fe^{II} ions.[4] The LS/HS Fe^{II} ratio is 80 : 20%, approximating to [1HS–3LS] spin state distribution (Fig. 6e). The Mössbauer spectrum of **3**·desolvated also exhibits two quadrupole doublets: [δ = 0.44 mm s^{-1}; ΔE_Q = 0.35 mm s^{-1}; A = 56%; blue] and [δ = 1.17 mm s^{-1}; ΔE_Q = 3.13 mm s^{-1}; A = 44%; red], corresponding to LS and HS Fe^{II} ions, respectively (Fig. 6c). The LS/HS Fe^{II} ratio is 56 : 44%, similar to that of **1** at 80 K [62% (δ = 0.45 mm s^{-1}; ΔE_Q = 0.36 mm s^{-1}) : 38% (δ = 1.17 mm s^{-1}; ΔE_Q = 3.12 mm s^{-1})] (Fig. 6a),[22] which is close to [2HS–2LS] spin states pattern and is consistent with the magnetic susceptibility analysis (Fig. 6d and f). Similar δ and ΔE_Q values can be observed in previously reported polynuclear Fe^{II} complexes with a FeN_6 coordination mode and no traces of Fe^{III} ions were detected.[4,22,41]

DFT calculations

In order to get a better understanding of the SCO behaviour of the cages, we applied density functional theory calculations using ORCA 5.0.[42] As the whole cage including anions would be too large to be studied computationally, first we modelled the $[Fe_4^{II}L_6]^{8+}$ core in the absence of anions in order to: (i)

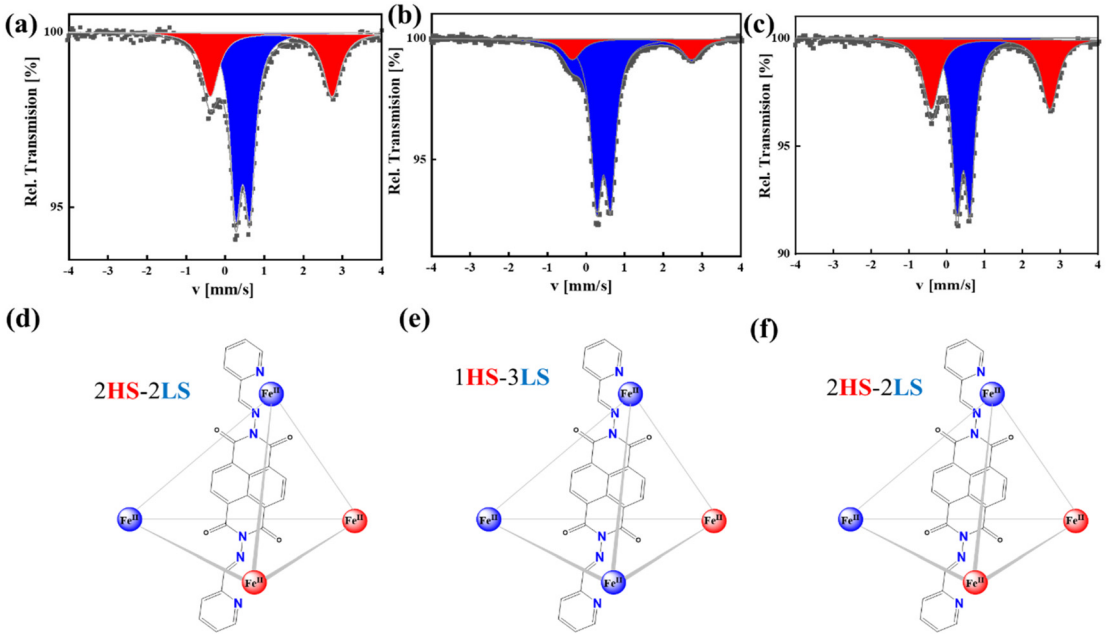

Fig. 6 ^{57}Fe Mössbauer spectra of desolvated samples **1** (a), **2** (b) and **3** (c) recorded at 80 K. The blue and red quadrupole doublets corresponding to LS and HS Fe^{II} ions, respectively. Schematic diagrams of the corresponding spin-state distribution in **1** (d), **2** (e) and **3** (f). Blue Fe^{II} centers: LS; Red Fe^{II} centers: HS; their locations are hypothetical.

check the effect of systematically changing the spin of one Fe centre on the structure and energy of the complexes; (ii) select a functional that best describes our system; (iii) compare the Mössbauer parameters of the various spin isomers with experimental data. Next, we used a simplified system with truncated ligands and a single iron centre to study the effect of the anions.

Thus, first we focused on the impact of the SCO on the whole molecular structure of $[Fe^{II}_4L_6]^{8+}$ complex cation. Due to the large number of atoms, the efficient BP86 functional was chosen for the geometry optimization for individual spin isomers labeled as 4LS, 3LS–1HS, 2LS–2HS, 1LS–3HS, and 4HS. Their molecular geometries are available in ESI.† The properties of the respective coordination polyhedra were evaluated with OctaDist[43] and are summarized in Table S4.† The average Fe–N distance increases from 1.964–1.965 Å in the LS state to 2.156–2.158 Å in the HS state, and is accompanied by the increase of Σ-parameters quantifying the distortion of octahedra from 59–60° to 88–89°. The volume change associated with SCO was also evaluated by calculating the volume of the tetrahedron defined by the atomic positions of four Fe atoms in each spin isomer of $[Fe^{II}_4L_6]^{8+}$ cage complex (Table S5†). Each spin state transition induces 0.8–1.1% volume change, and the volume increases from 226.4 Å^3 for 4LS to 235.2 Å^3 for 4HS. Next, single-point electronic energies were calculated for each spin isomer with hybrid functional B3LYP and with hybrid meta-GGA functional TPSSh. These calculations showed that the energy is increasing gradually from 4LS to 4HS and that the energy differences are almost equidistant for all spin transitions, but in magnitude vary significantly upon the applied DFT functional (BP86: ~34 kcal mol^{-1}, B3LYP: ~3.5 kcal mol^{-1}, TPSSh: ~18 kcal mol^{-1}, see Table S6†). The reasonably small value found by B3LYP is in accordance with the experimentally observed SCO behaviour. The calculated near-equal energy differences for each spin transition imply that the coupling between the various Fe centres is weak and they do not significantly influence the spin state change of each other and is also in very good accordance with the gradual change of the overall spin state evolution monitored by the magnetic measurements. The respective Mulliken and Löwdin spin populations on iron atoms correspond nicely to expected values for 4LS, 3LS–1HS, 2LS–2HS, 1LS–3HS, and 4HS individual spin isomers (Table S6 and Fig. S11†). Finally, DFT methods were used to provide information about ^{57}Fe Mössbauer spectroscopy parameters, namely the isomer shift (δ) and the quadrupole splitting (ΔE_Q) to validate the calculated geometries and properties. However, to our best knowledge, there is no DFT calibration study done using the new version of ORCA 5.0, which uses different numerical grids than previous versions for which several such studies are available. Nevertheless, we took inspiration from Pápai *et al.*[44] and selected iron(II) complexes with {FeN_6} chromophore in LS and HS state for which the calibration study was performed (Table S7 and Fig. S12†). This enabled us to calculate δ for all spin isomers of $[Fe^{II}_4L_6]^{8+}$ cage complex, which are reported in Table S8† and in Table 3 with B3LYP functional. Indeed, there is good agreement with the experimental parameters in Table 2, which: (i) implies that the effect of anions is indeed small on Mössbauer parameters; (ii) supports the reliability of the selected theoretical procedures.

Table 2 ^{57}Fe Mössbauer parameters for desolvated **1–3** samples

Samples	Spin state Fe(II)	A/A_{tot} (%)	Mössbauer parameters δ (mm s^{-1})	ΔE_Q (mm s^{-1})	$\Gamma/2$ (mm s^{-1})
1	LS (blue)	62	0.45	0.36	0.34
	HS (red)	38	1.17	3.12	0.52
2	LS (blue)	80	0.45	0.36	0.33
	HS (red)	20	1.19	3.09	0.58
3	LS (blue)	56	0.44	0.35	0.30
	HS (red)	44	1.17	3.13	0.52

Table 3 Calculated ^{57}Fe Mössbauer parameters for 4LS 3LS–1HS 2LS–2HS 1LS–3HS and 4HS spin isomers of $[Fe^{II}_4L_6]^{8+}$ cage complex from B3LYP functional

Spin isomer	Spin state	δ (mm s^{-1}) at 4.2 K	$\lvert\Delta E_Q\rvert$ (mm s^{-1})
4LS	LS	0.468	0.331–0.339
3LS–1HS	LS	0.465–0.468	0.325–0.344
	HS	1.063	3.394
2LS–2HS	LS	0.463–0.465	0.319–0.337
	HS	1.062–1.064	3.361–3.483
1LS–3HS	LS	0.463	0.325
	HS	1.057–1.062	3.353–3.444
4HS	HS	1.057–1.058	3.407–3.420

After having established that: (i) spin state changes of the Fe centres are practically independent of each other; (ii) B3LYP produces relative energy differences between HS, LS and mixed HS–LS states of the $[Fe^{II}_4L_6]^{8+}$ cage in accordance with SCO phenomenon, we concluded that B3LYP is the most reliable functional, and turned our attention towards the interaction between anions and the cage. To reduce the computational demand, we designed a model system including only one Fe centre and truncated ligands in the absence and presence of the anions (models **1–3** with anions BF_4^-, ClO_4^- and $CF_3SO_3^-$, respectively see structures in Fig. S13†). This smaller model also allowed us to take the effect of entropy into account. The results suggest that the anions interact with the ligands through the pyridine ring, mainly by C–H hydrogens. The local structure around the Fe centers is not significantly influenced by the nature of the cages as shown by the Fe–N distances (Table S9†), and this remark is valid in both spin states. The elongation of the Fe–N distances from LS to HS is perfectly reproduced by DFT. Interestingly, together with the elongation of the Fe–N distances in the HS state, the anions come slightly closer to the Fe center compared to the LS state.

The very similar electronic structure of the three cages was confirmed by comparing the molecular orbitals with and without anions. The iron d-orbitals (neither their shape, nor their energy) and the splitting between the t_{2g} and e_g orbitals are hardly affected (see Table S10 and Fig. S14†). This is further witnessed by the charges calculated for the various fragments in the systems (Table S11†). The iron charge is not affected by the nature of the anion contrary to the ligands with a slightly smaller electron transfer from ClO_4^- and $CF_3SO_3^-$ (~0.25 e^- per anion) towards the ligands compared to the smaller and harder BF_4^- (~0.3 e^- per anion).

The calculated Gibbs free energies for the HS and LS splitting of the three cages both by the B3LYP and B3LYP* functionals are in line with the experimentally observed SCO behavior. While spin state splittings are notoriously hard to estimate properly, it is well-established that increasing the Hartree–Fock (HF) exchange content of the functional will favor the HS state.[45] In accordance with this knowledge, the HS is favored by B3LYP (includes 20% HF exchange) and the LS by B3LYP* (15% HF exchange) for this truncated system. Both functionals fully agree that the difference between the HS and LS states of **1** and **3** is very similar (Table S12†) while **2** has a larger spin state splitting, in accordance with the experiments. *e.g.*, at the B3LYP/SVP level of theory the Gibbs free energy differences at 80 K between the LS–HS states of the three cages are the following **1**: 2.0 kcal mol^{-1}; **2**: −0.9 kcal mol^{-1}; **3**: 2.1 kcal mol^{-1}. The use of a larger basis set or inclusion of a solvent model in the calculations does not change this conclusion, giving further confidence to the obtained results.

To gain more insight into the larger stability of the LS state in **2**, the interaction energy between the Fe^{2+} complex with its ligands and the anions was calculated (Table S13†). Interaction energies depend significantly more on the size of the basis than geometries, and larger basis sets are expected to yield more reliable results. The data of Table S13† suggests (based on both functionals) that there is a larger difference between the interaction of the perchlorate anion with the Fe^{2+} complex in the HS and LS states than between those of the other two anions. *e.g.*, at the B3LYP/TZVP level interaction Gibbs free energy in the HS/LS states for the three cages are in kcal mol^{-1}: **1**: −188.2/−189.8; **2**: −193.9/−196.3; **3**: −188.4/−189.2. These results suggest that the slightly larger stability of the LS state in **2** (compared to **1** and **3**) may arise from the fact that the perchlorate anion presumably interacts more strongly with the LS state compared to the two other anions.

Conclusions

In conclusion, we have successfully synthesized two new Fe^{II} tetrahedral cages **2** and **3** by subcomponent self-assembly, utilizing the same pyridine–hydrazone ligand scaffold but with different anions (ClO_4^- and $CF_3SO_3^-$, respectively) to study solvent and counter anion effects on spin crossover properties based on **1** (BF_4^-). Single-crystal X-ray diffraction and electrospray ionization-time of flight-mass spectrometry analyses clearly demonstrate the tetrahedral cage structures and their discrete tetranuclear nature. Temperature-dependent $\chi_m T$ plots show that the presence of solvent molecules stabilizes the LS state in **1–3**, but does not have a dramatic effect on the transition temperatures as well as on the shape of the spin crossover profiles. The counter anions effect was studied among desolvated **1–3**. Magnetic data and ^{57}Fe Mössbauer spectral data show that the anions influence the spin-state distri-

butions of the Fe^{II} ions, and the cause of this phenomenon was systematically investigated by density functional theory calculations. Further studies on the influence of substituents on the spin crossover profiles are therefore anticipated in this new cage family.

Author contributions

WL and XL performed synthesis, characterization and wrote the manuscript with YG. KR collected crystallographic data. MW performed ESI-TOF-HRMS experiments. JK, JO and RH performed DFT calculations. SD and FM performed SQUID and ^{57}Fe Mössbauer spectroscopic measurements.

Conflicts of interest

There are no conflicts to declare.

Acknowledgements

This work was supported through the Fonds De La Recherche Scientifique—FNRS (PDR T.0095.21, CDR J.0168.22, CDR J.0064.23), the COST action CA21149 and the Deutsche Forschungsgemeinschaft (DFG, German Research Foundation) 217133147/SFB 1073, project B06 (to F. M.). W. Li and X. Li were supported by a fellowship from the China Scholarship Council (201908310083 and 202108310050). J. O. acknowledges financial support of the "Vissza a Tudományba" grant of Budapest University of Technology and Economics and of the NKFIH Grant No. 146661 of the National Research, Development and Innovation Office of Hungary, J. K. thanks the support of a Stipendium Hungaricum Fellowship of the Tempus Public Foundation. R. H. acknowledges the financial support from the institutional sources of the Department of Inorganic Chemistry, Palacký University Olomouc, Czech Republic. Purchase of the SQUID magnetometer was enabled by the Deutsche Forschungsgemeinschaft (DFG, German Research Foundation, project number INST 186/1329-1 FUGG) and the Niedersächsische Ministerium für Wissenschaft und Kultur (MWK)."

References

1 J. Linares, E. Codjovi and Y. Garcia, *Sensors*, 2012, **12**, 4479–4492.
2 C. Lefter, V. Davesne, L. Salmon, G. Molnár, P. Demont, A. Rotaru and A. Bousseksou, *Magnetochemistry*, 2016, **2**, 18.
3 P. Gütlich, A. Hauser and H. Spiering, *Angew. Chem., Int. Ed. Engl.*, 1994, **33**, 2024–2054.
4 P. Gütlich, Y. Garcia and H. A. Goodwin, *Chem. Soc. Rev.*, 2000, **29**, 419–427.
5 M. A. Halcrow, *Polyhedron*, 2007, **26**, 3523–3576.
6 M. A. Halcrow, *Spin-crossover materials: properties and applications*, John Wiley & Sons, 2013.
7 R. W. Hogue, S. Singh and S. Brooker, *Chem. Soc. Rev.*, 2018, **47**, 7303–7338.
8 J. Zheng, L. K. S. von Krbek, T. K. Ronson and J. R. Nitschke, *Angew. Chem., Int. Ed.*, 2022, **61**, e202212634.
9 A. J. McConnell, *Supramol. Chem.*, 2018, **30**, 858–868.
10 W. K. Han, H. X. Zhang, Y. Wang, W. Liu, X. Yan, T. Li and Z. G. Gu, *Chem. Commun.*, 2018, **54**, 12646–12649.
11 W. Li, L. Sun, C. Liu, A. Rotaru, K. Robeyns, M. L. Singleton and Y. Garcia, *J. Mater. Chem. C*, 2022, **10**, 9216–9221.
12 Z. Wang, L. P. Zhou, L. X. Cai, C. B. Tian and Q. F. Sun, *Nano Res.*, 2021, **14**, 398–403.
13 A. Ferguson, M. A. Squire, D. Siretanu, D. Mitcov, C. Mathoniere, R. Clérac and P. E. Kruger, *Chem. Commun.*, 2013, **49**, 1597–1599.
14 Y. Sunatsuki, R. Kawamoto, K. Fujita, H. Maruyama, T. Suzuki, H. Ishida, M. Kojima, S. Iijima and N. Matsumoto, *Coord. Chem. Rev.*, 2010, **254**, 1871–1881.
15 R. A. Bilbeisi, S. Zarra, H. L. Feltham, G. N. Jameson, J. K. Clegg, S. Brooker and J. R. Nitschke, *Chem. – Eur. J.*, 2013, **19**, 8058–8062.
16 D. H. Ren, D. Qiu, C. Y. Pang, Z. Li and Z. G. Gu, *Chem. Commun.*, 2015, **51**, 788–791.
17 H. X. Zhang, X. Yan, Y. X. Chen, S. H. Zhang, T. Li, W. K. Han, L. Y. Bao, R. Shen and Z. G. Gu, *Chem. Commun.*, 2019, **55**, 1120–1123.
18 F. L. Zhang, J. Q. Chen, L. F. Qin, L. Tian, Z. Li, X. Ren and Z. G. Gu, *Chem. Commun.*, 2016, **52**, 4796–4799.
19 L. Li, N. Saigo, Y. Zhang, D. J. Fanna, N. D. Shepherd, J. K. Clegg, R. Zheng, S. Hayami, L. F. Lindoy and J. R. Aldrich-Wright, *J. Mater. Chem. C*, 2015, **3**, 7878–7882.
20 T. Tanaka, Y. Sunatsuki and T. Suzuki, *Inorg. Chim. Acta*, 2020, **502**, 119373.
21 L. Li, A. R. Craze, O. Mustonen, H. Zenno, J. J. Whittaker, S. Hayami, L. F. Lindoy, C. E. Marjo, J. K. Clegg and J. R. Aldrich-Wright, *Dalton Trans.*, 2019, **48**, 9935–9938.
22 W. Li, C. Liu, J. Kfoury, J. Oláh, K. Robeyns, M. L. Singleton, S. Demeshko, F. Meyer and Y. Garcia, *Chem. Commun.*, 2022, **58**, 11653–11656.
23 M. Steinert, B. Schneider, S. Dechert, S. Demeshko and F. Meyer, *Inorg. Chem.*, 2016, **55**, 2363–2373.
24 M. Fumanal, F. Jimenez-Gravalos, J. Ribas-Arino and S. Vela, *Inorg. Chem.*, 2017, **56**, 4474–4483.
25 R. J. Archer, H. S. Scott, M. I. Polson, C. Mathonière, M. Rouzières, R. Clérac and P. E. Kruger, *Chem. – Asian. J.*, 2019, **14**, 2225–2229.
26 M. M. Dirtu, A. Rotaru, D. Gillard, J. Linares, E. Codjovi, B. Tinant and Y. Garcia, *Inorg. Chem.*, 2009, **48**, 7838–7852.
27 M. M. Dîrtu, C. Neuhausen, A. D. Naik, A. Rotaru, L. Spinu and Y. Garcia, *Inorg. Chem.*, 2010, **49**, 5723–5736.
28 R. J. Archer, H. S. Scott, M. I. Polson, B. E. Williamson, C. Mathonière, M. Rouzières, R. Clérac and P. E. Kruger, *Dalton Trans.*, 2018, **47**, 7965–7974.

29 A. R. Craze, H. Zenno, M. C. Pfrunder, J. C. McMurtrie, S. Hayami, J. K. Clegg and F. Li, *Inorg. Chem.*, 2021, **60**, 6731–6738.
30 A. R. Craze, N. F. Sciortino, M. M. Badbhade, C. J. Kepert, C. E. Marjo and F. Li, *Inorganics*, 2017, **5**, 62.
31 A. R. Craze, M. M. Bhadbhade, C. J. Kepert, L. F. Lindoy, C. E. Marjo and F. Li, *Crystals*, 2018, **8**, 376.
32 M. Steinert, B. Schneider, S. Dechert, S. Demeshko and F. Meyer, *Angew. Chem.*, 2014, **126**, 6249–6253.
33 Y. T. Wang, S. T. Li, S. Q. Wu, A. L. Cui, D. Z. Shen and H. Z. Kou, *J. Am. Chem. Soc.*, 2013, **135**, 5942–5945.
34 R. Dine-Hart, *J. Polym. Sci., Part A: Polym. Chem.*, 1968, **6**, 2755–2764.
35 T. K. Ronson, S. Zarra, S. P. Black and J. R. Nitschke, *Chem. Commun.*, 2013, **49**, 2476–2490.
36 L. Sun, M. Ndiaye, N. El Islam Belmouri, K. Robeyns, A. Rotaru, K. Boukheddaden and Y. Garcia, *Cryst. Growth Des.*, 2022, **22**, 7555–7563.
37 W. Y. Zhang, Y. F. Han, L. H. Weng and G. X. Jin, *Organometallics*, 2014, **33**, 3091–3095.
38 H. C. Liang, Y. Pan, H. L. Zhu, Y. S. Meng, C. H. Liu, T. Liu and Y.Y. Zhu, *Inorg. Chem. Front.*, 2022, **9**, 2343–2352.
39 S. Xue, Y. Guo, A. Rotaru, H. Müller-Bunz, G. G. Morgan, E. Trzop, E. Collet, J. Oláh and Y. Garcia, *Inorg. Chem.*, 2018, **57**, 9880–9891.
40 A. J. Scott, J. Vallejo, A. Sarkar, L. Smythe, E. Regincós Martí, G. S. Nichol, W. T. Klooster, S. J. Coles, M. Murrie, G. Rajaraman, S. Piligkos, P. J. Lusby and E. K. Brechin, *Chem. Sci.*, 2021, **12**, 5134–5142.
41 M. Nihei, T. Shiga, Y. Maeda and H. Oshio, *Coord. Chem. Rev.*, 2007, **251**, 2606–2621.
42 F. Neese, *Wiley Interdiscip. Rev.: Comput. Mol. Sci.*, 2022, **12**, e1606.
43 R. Ketkaew, Y. Tantirungrotechai, P. Harding, G. Chastanet, P. Guionneau, M. Marchivie and D. J. Harding, *Dalton Trans.*, 2021, **50**, 1086–1096.
44 M. Pápai and G. Vankó, *J. Chem. Theory Comput.*, 2013, **9**, 5004–5020.
45 J. N. Harvey, *Annu. Rep. Prog. Chem., Sect. C*, 2006, **102**, 203–226.